Forbidden transitions in one- and two-electron nickel

R. W. Dunford, H. G. Berry, D. A. Church,* M. Hass,† C. J. Liu,‡ M. L. A. Raphaelian,§ and
B. J. Zabransky

Physics Division, Argonne National Laboratory, Argonne, Illinois 60439

L. J. Curtis

Department of Physics and Astronomy, University of Toledo, Toledo, Ohio 43606

A. E. Livingston

Department of Physics, University of Notre Dame, Notre Dame, Indiana 46556
(Received 3 May 1993)

We describe measurements of the lifetimes of metastable states in one- and two-electron nickel ions. The $2\,^2S_{1/2}$ level in one-electron nickel was found to have a lifetime of 217.1(1.8) ps, in agreement with a theoretical calculation of 215.45 ps. The lifetimes of the $2\,^1S_0$ and $2\,^3P_2$ levels in two-electron nickel were found to be 156.1(1.6) and 70(3) ps, respectively, in agreement with the theoretical results of 154.3(0.5) and 70.6 ps. We also studied the phenomenon of hyperfine quenching of the He-like $2\,^3P_0$ level by comparing decay curves for the isotopes ^{61}Ni and ^{58}Ni. The lifetime of the $2\,^3P_0$ level in ^{61}Ni^{26+} was found to be 470(50) ps, in agreement with a theoretical prediction. The measurements were carried out using the beam-foil time-of-flight technique with a fast beam of highly charged nickel ions. We discuss the handling of systematic effects in the measurements, including the study of yrast cascades following the beam-foil interaction.

PACS number(s): 32.70.Fw, 31.30.Jv, 31.10.+z

I. INTRODUCTION

In several short articles [1–3] we have presented results of measurements of decay rates for four forbidden transitions in H-like and He-like nickel. In this article, we give a more complete account of these experiments with an emphasis on systematic errors and present some results including a study of the yrast cascades populating the $2p$ levels in one-electron nickel. We have studied the decay rates of the H-like $2\,^2S_{1/2}$ state and the He-like $2\,^1S_0$, $2\,^3P_2$, and $2\,^3P_0$ states. These states are produced using beam-foil excitation of a fast beam. One of the problems in the study of forbidden transitions is in dealing with the long lifetimes involved. However, the lifetimes of these states become shorter as the nuclear charge of the ions increases. For nickel [$Z=28$], the lifetimes of the states we are studying correspond to decay lengths on the order of 1 cm, a convenient measurement regime. For higher-Z ions, typical decay lengths are much shorter and experiments again become more difficult since they require working close to the excitation foil.

After briefly reviewing the present status of the theory for lifetimes of the $n=2$ levels of one- and two-electron nickel in Sec. II, we describe the experimental details in Sec. III. In Sec. IV, we analyze the efficiency of the experimental apparatus and develop relations used in optimizing the experimental geometry. In Sec. V, we discuss the results for each of the measurements emphasizing systematic effects. Finally, in Sec. VI we review the existing experimental data for these levels and compare them with the results of theory.

II. THEORY

Figure 1 shows the low-lying energy levels for H-like and He-like nickel including their lifetimes and decay modes. In this section we will review the current status of the theoretical calculations of the forbidden transitions in these ions. For more details see the review by Marrus and Mohr [4] and references therein.

A. Two-photon decays

Goeppert-Mayer [5] developed the formalism for two-photon decay and predicted that this was the primary decay mode for the $2s\,^2S_{1/2}$ level of hydrogen. Breit and Teller [6] studied the decay rates of the low-lying levels of hydrogen and helium and confirmed Goeppert-Mayer's prediction. Accurate nonrelativistic calculations for hydrogen and one-electron ions have been made by Spitzer and Greenstein [7], Shapiro and Breit [8], Zon and Rapoport [9], Klarsfeld [10,11], and Drake [12]. These calculations showed that the emitted photons have a continuous energy distribution with the sum of the energies of the two photons E_1 and E_2 adding up to the transition energy E_0:

$$E_0 = E_1 + E_2 . \tag{1}$$

The nonrelativistic decay rate ω as a function of angle and energy has the form [4]

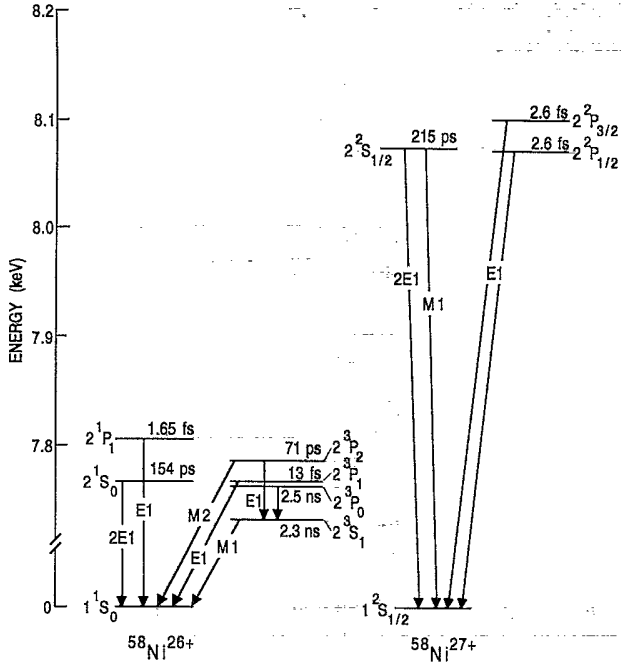$$\frac{d^3\omega}{dy\,d\Omega_1 d\Omega_2} = (Z\alpha)^6 (1+\cos^2\theta)\chi(y) , \tag{2}$$

FIG. 1. Low-lying energy levels for H-like and He-like ^{58}Ni showing lifetimes and decay modes.

where θ is the angle between the two photons, Z is the nuclear charge,

$$y = \frac{E}{E_0} , \qquad (3)$$

and $\chi(y)$ is a function with a broad maximum at $y = \frac{1}{2}$ which drops to zero at $y = 0$ and 1. Note that, in this nonrelativistic limit, the spectral shape is not dependent on the nuclear charge. After integrating over angles and energy, Drake's result for the nonrelativistic decay rate is

$$\omega_{nr}^{2\,^2S_{1/2}2E1} = 8.229\,38Z^6 \text{ s}^{-1} , \qquad (4)$$

which for nickel gives

$$\omega_{nr}^{2\,^2S_{1/2}2E1} = 3.966 \times 10^9 \text{ s}^{-1} . \qquad (5)$$

Parpia and Johnson [13,14] and Goldman and Drake [15,16] have made fully relativistic calculations. The former calculations include finite-nuclear-size effects. Johnson [13] presents a tabulation of the frequency distribution $\psi(y,Z)$ defined by

$$\frac{d\omega_{rel}^{2\,^2S_{1/2}2E1}}{dy} = Z^6(9\alpha^6/2^{10})\psi(y,Z) \text{ Ry} . \qquad (6)$$

With the inclusion of relativistic corrections, the shape depends on the nuclear charge Z. Drake [12] fit his relativistic results for the total decay rate to an empirical formula to obtain

$$\omega_{rel}^{2\,^2S_{1/2}2E1}$$
$$= 8.229\,38Z^6Z_r^4(1+m/M)$$
$$\times \frac{[1+3.9448(\alpha Z)^2 - 2.040(\alpha Z)^4]}{[1+4.6019(\alpha Z)^2]} \text{ s}^{-1} , \qquad (7)$$

where

$$\bar{Z}_r = \frac{(Z-n)m}{M+nm} + 1 . \qquad (8)$$

Here n is the number of electrons in the ion, m is the electron mass, and M is the mass of the nucleus. Equation (7) is good to within 0.005% up to $Z = 92$. This result includes finite-nuclear-mass and nuclear-recoil [17,18] corrections. Using this formula for $Z = 28$ gives

$$\omega_{rel}^{2\,^2S_{1/2}2E1} = 3.868 \times 10^9 \text{ s}^{-1} . \qquad (9)$$

Dalgarno [19,20] made the first calculation of the two-photon decay rate of the $2\,^1S_0$ level for helium. Other nonrelativistic calculations for helium and He-like ions have been completed by Victor [21,22], Jacobs [23], and Drake [24,12]. Drake expressed his result with the formula

$$\omega_{nr}^{2\,^1S_0} = 16.458\,762(Z - 0.806\,389)^6$$
$$\times \left[1 + \frac{1.539}{(Z+2.5)^2}\right] \text{ s}^{-1} . \qquad (10)$$

For nickel, this gives the nonrelativistic decay rate

$$\omega_{nr}^{2\,^1S_0} = 6.667 \times 10^9 \text{ s}^{-1} . \qquad (11)$$

Drake [12] also estimated the relativistic corrections to this decay rate. His result for the decay rate in He-like nickel including relativistic corrections is

$$\omega_{rel}^{2\,^1S_0} = 6.482 \times 10^9 \text{ s}^{-1} . \qquad (12)$$

B. Magnetic dipole decay

The H-like decay of the $2\,^2S_{1/2}$ level also has a single-photon magnetic dipole mode. This mode is highly suppressed, and it vanishes if the nonrelativistic wave functions are used. Johnson [13] obtained a "nonrelativistic" result

$$\omega_{nr}^{2\,^2S_{1/2}M1} = 2.496 \times 10^{-6}Z^{10} \text{ s}^{-1} \qquad (13)$$

by calculating the $M1$ matrix element in the Dirac theory and taking the nonrelativistic limit. For nickel, this gives

$$\omega_{nr}^{2\,^2S_{1/2}M1} = 7.393\,07 \times 10^8 \text{ s}^{-1} . \qquad (14)$$

The nonrelativistic results in Eqs. (5) and (14) yield a lifetime of 212.54 ps and a branching ratio

$$b_{nr} = \frac{\omega_{nr}^{2\,^2S_{1/2}M1}}{\omega_{nr}^{2\,^2S_{1/2}2E1} + \omega_{nr}^{2\,^2S_{1/2}M1}} = 0.1571 . \qquad (15)$$

Fully relativistic calculations [15,14,16] yield a lifetime of 215.45 ps and a branching ratio

$$b_{rel} = 0.1667 . \qquad (16)$$

C. Magnetic quadrupole decay

At low Z, the $2\,^3P_2$ level in He-like ions decays mostly by an electric dipole transition to the $2\,^3S_1$ level, but

above about $Z = 17$, the magnetic quadrupole transition to the ground state dominates. This is because the $M2$ transition probability increases as Z^8, while the $E1$ transition probability increases only linearly with Z. Nonrelativistic calculations of the $M2$ decay rate have been made by Mizushima [25], Garstang [26,27], Drake [28,29], and Jacobs [30]. Relativistic corrections have been calculated by Gould, Marrus, and Mohr [31] and Johnson and co-workers [32–34]. The latter used the relativistic-random-phase approximation (RRPA) to calculate both the $M2$ and the $E1$ transition probabilities. The RRPA results for He-like nickel are

$$\omega_{\text{rel}}^{2\,^3P_2\,M2} = 1.20 \times 10^{10} \text{ s}^{-1} \, , \tag{17}$$

$$\omega_{\text{rel}}^{2\,^3P_2\,E1} = 2.17 \times 10^{9} \text{ s}^{-1} \, , \tag{18}$$

corresponding to a lifetime

$$\tau_{\text{rel}}^{2\,^3P_2} = 70.6 \text{ ps} \, , \tag{19}$$

and a branching ratio

$$b_{\text{rel}}^{2\,^3P_2} = \frac{\omega_{\text{rel}}^{2\,^3P_2\,M2}}{\omega_{\text{rel}}^{2\,^3P_2\,E1} + \omega_{\text{rel}}^{2\,^3P_2\,M2}} = 0.847 \, . \tag{20}$$

D. Hyperfine quenching

In the absence of hyperfine structure, the $2\,^3P_0$ state decays to the $2\,^3S_1$ state by an $E1$ transition. The RRPA result for the lifetime of the $2\,^3P_0$ level in $^{58}\text{Ni}^{26+}$ is

$$\tau_{\text{rel}}^{2\,^3P_0\,E1} = 2.30 \text{ ns} \, . \tag{21}$$

In $^{61}\text{Ni}^{26+}$, which has nuclear spin, mixing by the hyperfine interaction alters the decay rates of both the $2\,^3P_0$ and the $2\,^3P_2$ levels. These are mixed with the short-lived $2\,^1P_1$ and $2\,^3P_1$ states, opening up decay channels to the ground state and shortening their lifetimes. This phenomenon of hyperfine quenching was first discussed by Bowen [35] in 1930, and observed in 1937 by Mrozowski [36], in experiments in Hg I. Gould, Marrus, and Mohr [31] first observed hyperfine quenching in the He-like ions. Calculations of decay rates for $2\,^3P_0$ have been made by Mohr [37], Indelicato, Parente, and Marrus [38], and Munger [39].

III. EXPERIMENT

A schematic of the Argonne Tandem Van de Graaff–Linac (ATLAS) and the Atomic Physics Beamline where the experiments were carried out is shown in Fig. 2. Nickel beams with energies of 340, 346, 376, 664, and 670 MeV were used in four separate runs of 3–4 days each. The beams were stripped in 200–500-μg/cm^2 foil targets located just in front of the switching magnet. Depending on the measurement, we directed the 26+, 27+, or 28+ charge state into our target chamber.

A schematic of the detector arrangement in our target chamber is shown in Fig. 3. The major components were three Si(Li) detectors and a movable foil target. There
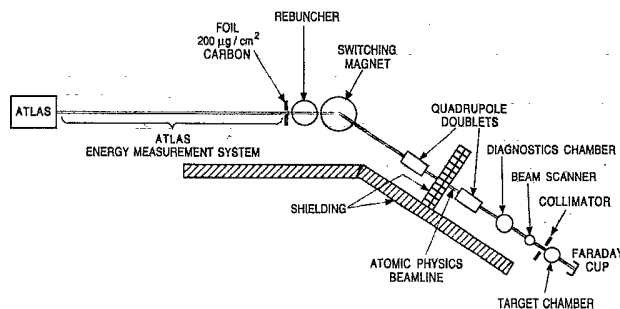

FIG. 2. Beamline arrangement.

was also a normalization detector which moved with the target. Lifetimes were measured using the beam-foil time-of-flight technique in which the foil was moved relative to the region along the beam that was viewed by the detectors. Two of the detectors (1 and 2) were collimated so that they observed a region of about 5 mm along the beam. Detector 3 was less collimated and had a larger solid angle.

Several considerations were used in choosing the detector arrangement. The detectors had to be close to the beam to maximize the solid angle, but not so close that
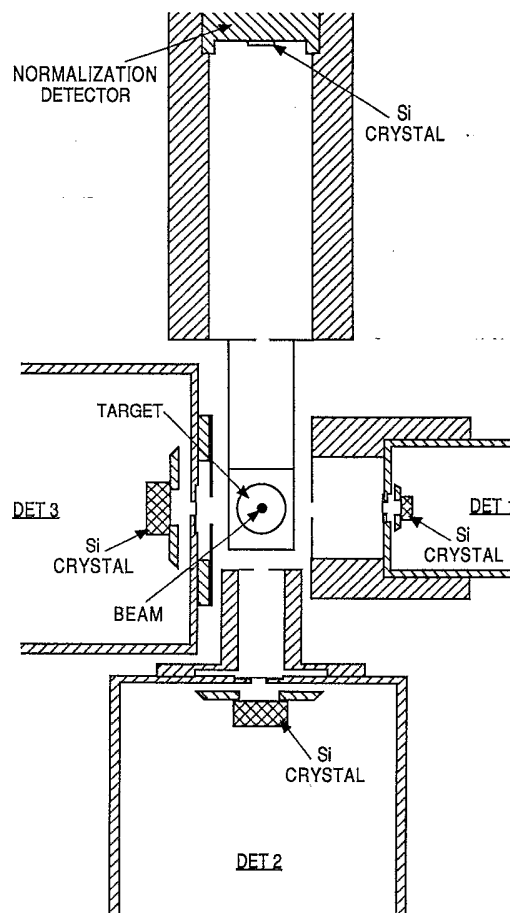

FIG. 3. Schematic of target chamber showing positions of three Si(Li) detectors and the normalization detector. The beam direction is out of the page. The normalization detector and the target foil move along the beam.

the solid angle was sensitive to slight transverse movements of the centroid of the beam that would contribute to signal fluctuations. The collimators were chosen to optimize the coincidence rate for the measurements of the two-photon decays and they mainly restricted the field of view along the beam. An important requirement was that the two collimated detectors should not be able to "see" the foil (as well as upbeam of the foil) when it was brought to its closest position to the detectors. Otherwise, the detector solid angle could change as the foil was moved. Another factor was that the "beam spot" (region of interaction of the beam on the foil) was a relatively intense source of x rays, so it was desirable to avoid viewing it in order to reduce the count rates in the detectors. For detector 3, we relaxed the requirement that the detector not view the foil. The rate in this detector was reduced by filtering out intense low-energy lines (<2 keV). Also, this detector was always used in coincidence with detector 1 or 2, so the requirement for restricting the region along the beam that was being viewed was satisfied by the coincidence condition. Detector 3 was not used for any of the singles decay curves, but with its relatively high solid angle it was essential for the coincidence measurements.

In order to determine the lifetime, we precisely measured both the relative foil position and the beam velocity. The beam velocity was determined using the ATLAS time-of-flight energy-measurement system [40]. This is located in the straight section of beamline between the exit of ATLAS and the switching magnet (see Fig. 2). This system is capable of determining the beam energy to about 0.1%. We also considered the energy loss of the beam in the two foils. This was a small correction that we determined using standard tables [41] of energy loss in materials and measurements of the foil thicknesses using an alpha radiation source.

The normalization detector was attached to the stage that translates the foil and therefore observed a fixed region downstream of the foil. This detector was an ion-implanted passivated silicon detector. It was located entirely within the vacuum chamber and was uncooled. The resolution was 1.8 keV at 14.4 keV. This detector was located 10 cm from the beam axis which made the normalization less sensitive to transverse beam movement or misalignment of the beam relative to the translation axis of the stage. The latter was important to ensure that the solid angle of the normalization detector did not change as the foil was translated along the beam.

Detectors 1, 2, and 3 were lithium-drifted silicon detectors cooled to liquid-nitrogen temperature. They were all fitted with beryllium windows which separated the vacuum of the detectors from the vacuum of the chamber. A number of different Si(Li) detector configurations were used in these experiments. Table I gives the properties of the detectors and their physical dimensions for the configuration shown in Fig. 3, which was typical. Mylar filters were used to reduce the count rate of low-energy x rays in detector 3 and in the normalization detector. The thicknesses of these and the other absorbing layers are given in Table I.

Data acquisition and control of the foil position were completely automated. At each position of the foil, we took data for a fixed amount of charge collected at a Faraday cup that was located about 1 m downbeam of our apparatus. The data were taken using event mode recording. There were two different types of events. One was caused by a coincidence between any combination of detectors 1, 2, or 3, and the other was caused by any single detector firing. For the experiments designed to measure the two-photon coincidences, all coincidence events and normalization events were recorded and put on tape, but only a sample of the single counts in detectors 1, 2, and 3 was recorded.

Standard digital counting electronics were used for the experiment. An important consideration for the lifetime measurements was to control any count-rate-dependent effects such as dead time or pileup. Also, for the coincidence measurements we had to handle accidental coincidences. The signal from each preamp was split and sent to both fast and slow amplifiers. The fast amplifiers had rise times of about 50 ns and were used to generate the timing and gating signals. The slow amplifiers had rise times of 6 μs, except for that used with the normalization detector which had a rise time of 0.5 μs. In order to

TABLE I. Detector geometry and characteristics.

Quantity	Detector			
	1	2	3	Norm.
Detector dimensions (mm)				
Active diameter (Si crystal)	4	6	6	5
Sensitive depth (Si crystal)	3.0	5.27	5.27	0.3
Beam to Si crystal distance	35	47	22	100
Collimator slit[a]	5×5	5×5	5.5×5	5×3.8
Beam to collim. distance	12	14	12	40
Absorbing layers (μm)				
Be window	25.4	25.4	25.4	0.0
Au layer	0.02	0.02	0.02	0.02
Inactive Si layer	0.1	0.1	0.1	0.0
Mylar	0	0	175	125

[a]The shorter dimension is parallel to the beam direction.

eliminate dead-time effects, all detectors and the Faraday cup signal were gated off 1 μs after any of the detectors fired and remained gated out until the computer and all electronic modules were ready to receive another event. This forced all detectors to have the same dead time to within 1 μs per event. The 1-μs delay allows for recording coincident events.

If two signals were received in any detector during a characteristic time of about six times the rise time of the slow amplifier, the energy measurement for that event was not considered to be reliable. Since the energy measurement was used to identify a given decay mode, and since the fraction of events that were piled up increased with the event rate, this effect could have distorted the decay curves and caused an error in the lifetime measurement. In order to handle this problem, a pileup detection circuit was used which tagged events for which two fast signals were received from the same detector within 36 μs. Such events were recorded but rejected in data analysis. The rates at each foil position were corrected for the fraction of rejected events.

The detectors were calibrated using radioactive sources that produce x rays in the range of interest. These include ^{55}Fe, ^{57}Co, ^{65}Zn, and ^{54}Mn. A typical calibration spectrum for detector 1 is shown in Fig. 4.

IV. DETECTOR EFFICIENCY

The success of these experiments depended critically on the detector efficiency and the coincidence efficiency of the apparatus. Since the detector count rates were expected to be low, we developed a computer model for the experiment and used it to optimize the geometrical arrangement of the detectors and collimators. In this section we present some of the relations used in the analysis. These relations are also used in the data analysis discussed in Sec. V.

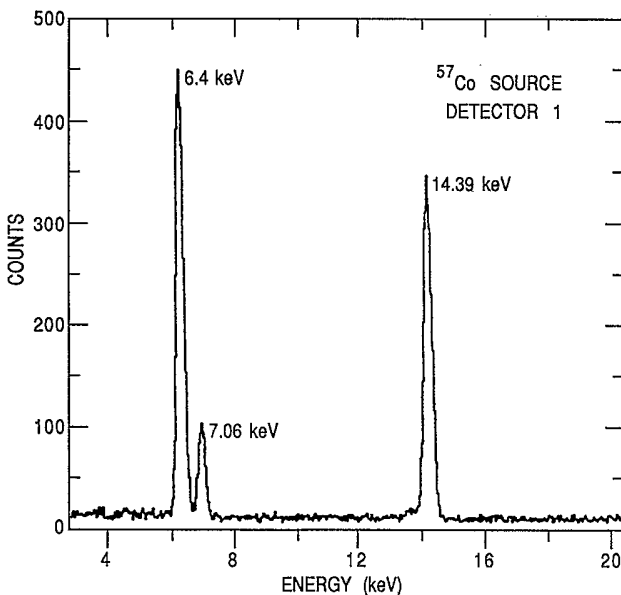The rate of detection of photons in detector i from a

FIG. 4. Calibration spectrum for Si(Li) detector 1.

decay mode l of an ion in length of beam dz at z for photons emitted in the energy interval dE at E is

$$N_i^l(z,E)dz\,dE$$

$$=R_l(z)dz\frac{\Omega_i(z-z_d)}{4\pi}A_i^l(z-z_d)\epsilon_i(E)D_l(E)dE\ ,\quad (22)$$

where $R_l(z)dz$ is the number of decays per second in dz for the mode and $\Omega_i(z-z_d)$ is the solid angle of detector i located at position z_d for photons emitted at z. We take $z=0$ to be the foil and imagine that the detectors can be translated together along the z axis (this is equivalent to a translation of the foil). The function $A_i^l(z-z_d)$ corrects the detector solid angle for anisotropic decay radiation from aligned states. This function is determined by averaging the angular distribution for photons emitted at z over the detector geometry. The parameter $\epsilon_i(E)$ is the fraction of incident photons of energy E that are detected. This parameter depends on the intrinsic efficiency of the detector and accounts for the absorption of photons before reaching the active silicon layer. The distribution $D_l(E)dE$ gives the fraction of photons of energy E in dE for a given decay mode. For a single-photon line, this is just the natural line shape. For the H-like two-photon decay, it can be expressed in terms of the spectral distribution $\psi(y,Z)$ defined by Johnson [13]:

$$D_{2E1}(E)=\frac{2\psi(y,Z)}{\int_0^1 \psi(y,Z)dy}\ ,\quad (23)$$

where

$$y=\frac{E}{E_0}\ ,\quad (24)$$

E_0 is the end-point energy, and Z is the nuclear charge. $D_{2E1}(E)$ is normalized so that

$$\int_0^{E_0}D_{2E1}(E)dE=2\ ,\quad (25)$$

that is, two photons for each decay. The singles rate for two-photon events in detector i at position z_d integrated over energies from E_a to E_b is

$$N_i^{2E1}(z_d)=\int_0^\infty R_{2E1}(z)\frac{\Omega_i(z-z_d)}{4\pi}dz$$
$$\times\int_{E_a}^{E_b}\epsilon_i(E)D_{2E1}(E)dE\ .\quad (26)$$

The alignment factor does not appear since the orbital angular momentum is zero. For the coincidence rate between detectors i and j, we consider the probability for each photon detected in i that the second photon is detected by j. This is

$$N_{ij}^{2E1}(z_d)=\int_0^\infty R_{2E1}(z)\frac{\Omega_i(z-z_d)}{4\pi}\frac{\Omega_j(z-z_d)}{4\pi}$$
$$\times K_{ij}^{2E1}(z-z_d)dz$$
$$\times\int_{E_a}^{E_b}\epsilon_i(E)\epsilon_j(E_0-E)D_{2E1}(E)dE\ ,\quad (27)$$

where $K_{ij}^{2E1}(z-z_d)$ accounts for the angular correlation

between the two photons averaged over the acceptance of detectors i and j.

Equations (26) and (27) can be used to estimate the singles and coincidence rates for the H-like and He-like two-photon emitters. The intrinsic detection efficiencies are dominated by the absorption of x rays in the absorbing layers listed in Table I. A complete discussion including a plot of detection efficiency versus x-ray energy is given in Ref. [42]. For the H-like $2\,^2S_{1/2}$ level, the yield was about 10^{-3} per Ni^{28+} ion for the 12-μg/cm^2 carbon target, and the yield of $2\,^1S_0$ states with a Ni^{26+} beam on this target was about $\frac{1}{3}$ of this. Typical currents for the 664-MeV nickel beams were 0.35 particle nA for Ni^{26+} and 0.05 particle nA for Ni^{28+}. Using these beam currents and the theoretical lifetimes we find

$$R_{2E1}^{2\,^2S_{1/2}}(z)=3\times10^5 e^{-0.998z}\ s^{-1}\,cm^{-1}\ , \tag{28}$$

$$R_{2E1}^{2\,^1S_0}(z)=9\times10^5 e^{-1.4z}\ s^{-1}\,cm^{-1}\ . \tag{29}$$

For the closest foil positions used in the experiments z_d is about 0.5 cm. Evaluating Eq. (26) for detector 1 at this foil position by numerical integration, we find singles two-photon event rates of 100 Hz for the H-like case and 250 Hz for the He-like case. Using Eq. (27), the two-photon coincidence rates for detectors 1 and 3 are calculated to be about 0.5 Hz for the Ni^{28+} beam on target and about 1 Hz for the Ni^{26+} beam on target. All of these rates are similar to what we observed in the experiments.

Next we consider cascade transitions, in particular a $3d\rightarrow2p$ decay followed by a $2p\rightarrow1s$ decay. Such decays contribute to the single-photon $M1$ line and they need to be understood in order to fit the decay curve formed from these lines. As discussed in Sec. V, the coincidence condition provides additional information on these decays. The analysis is similar to that used for the two-photon decays. The singles rate in the detector for the $3d\rightarrow2p$ line is given by

$$N_i^{3d2p}(z_d)=\epsilon_i(E_{3d2p})\int_0^\infty R_{3d2p}(z)dz$$
$$\times\Omega_i(z-z_d)A_i^{3d2p}(z-z_d)\ , \tag{30}$$

with a similar expression for the singles $2p\rightarrow1s$ line. For the yrast coincidence rate with the $3d\rightarrow2p$ decay photon detected in detector i and the $2p\rightarrow1s$ decay photon detected in detector j, we have

$$N_{ij}^{3d1s}(z_d)=\epsilon_i(E_{3d2p})\epsilon_j(E_{2p1s})$$
$$\times\int_0^\infty R_{3d2p}(z)\Omega_i(z-z_d)\Omega_j(z-z_d)$$
$$\times K_{ij}^{3d1s}(z-z_d)dz\ , \tag{31}$$

where $K_{ij}^{3d1s}(z-z_d)$ corrects for anisotropic emission due to initial alignment and angular correlation between the two photons both averaged over the acceptance of detectors i and j. In this expression, we assume that both decays $3d\rightarrow2p$ and $2p\rightarrow1s$ occur at the same position z. This is well justified for cascades through the short-lived $2p$ states. For the case of H-like nickel at 664 MeV, for example, the decay length of the $2p$ states is 0.1 μm.

We can examine the angular correlation in the cascade $3d\rightarrow2p\rightarrow1s$ using the formulas given by Biedenharn and Rose [43]. From their Eqs. (68) and (69) and their Table I(k), assuming statistical populations of the initial $3\,^2D_{5/2}$ and $3\,^2D_{3/2}$ levels we find the angular correlation to be

$$\omega(\theta)\propto(1+0.05\cos^2\theta)\ . \tag{32}$$

Since the coefficient of $\cos^2\theta$ is small, the angular correlation is not too important. A full analysis including the effect of alignment is needed for a complete description of this process [44], but we have no experimental information on alignment for our beams. The subject of the transfer of alignment in cascade transitions is discussed by Lin and Macek [45].

V. RESULTS

A. Singles spectra

Figure 5 shows spectra from detector 1 with a beam of fully stripped $^{58}Ni^{28+}$ ions incident on the target at an energy of 664 MeV. Two different foil positions are shown which illustrate the change in the spectrum as the foil is moved. The intense peak near 8 keV resolves into components from He-like and H-like transitions from $n=2$ levels. There are also intense lines near 1.5 keV that arise from transitions from $n>2$ into $n=2$. These lines persist to long decay times, so they must be fed by cascades from high-n levels. The continuum in the 2–7-keV region is largely due to two-photon decays, but other processes such as x-ray scattering and tails from higher-energy lines also contribute to this region and it is difficult to separate these background processes from the two-photon decays.

Figure 6 is a plot of spectra from detector 1 for He-like $^{58}Ni^{26+}$ incident on the target. In this case the intense line at 7.8 keV is mostly due to decay of He-like ions with little contribution from decays of H-like ions. The foil
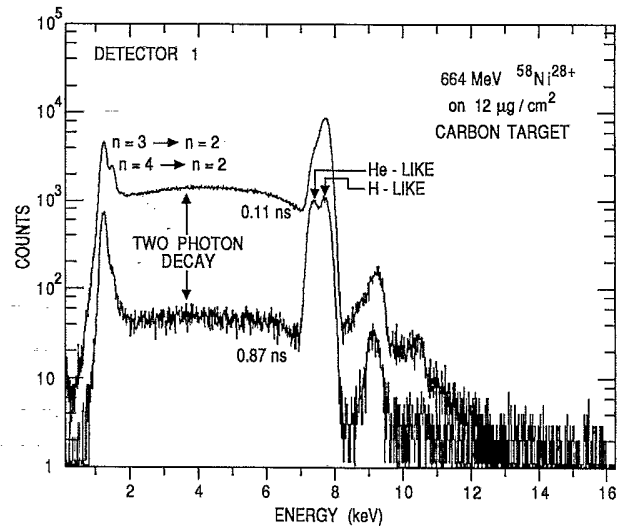
FIG. 5. Energy spectrum from detector 1 at two different foil positions corresponding to 0.11 and 0.87 ns beam travel time from the foil to the field of view of the detectors. Data obtained with 664-MeV $^{58}Ni^{28+}$ incident on the target.
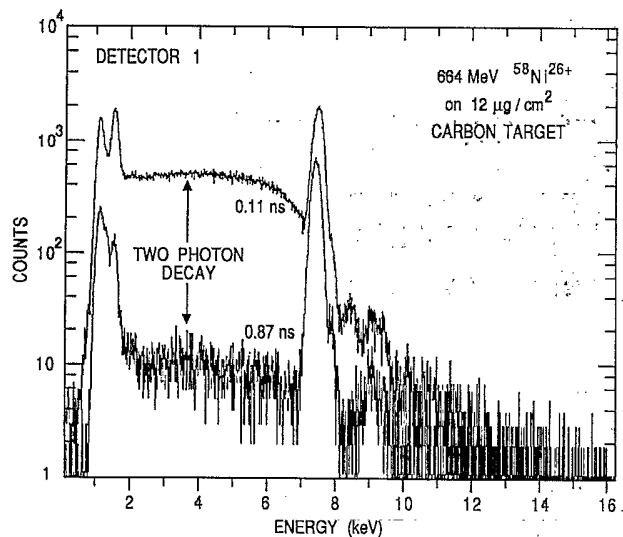
FIG. 6. Same as Fig. 5, but for 664-MeV ^{58}Ni^{26+} ions incident on the target.

positions in this figure are the same as in Fig. 5. The lower intensity in the continuum at 0.87 ns after excitation as compared to Fig. 5 is expected if the counts in this region are dominated by the decay of the He-like $2\,^1S_0$ state which has a shorter lifetime than the $2\,^2S_{1/2}$ level which dominates the continuum in the spectra of Fig. 5.

B. Yields vs foil thickness

In Fig. 7 we show the yield of photons versus foil thickness for the two-photon continuum and for the line at 7.8 keV. These data were taken with 340-MeV Ni^{26+} on target and are counts per μC in one of the Si(Li) detectors at the closest foil position. Under these conditions, the continuum is dominated by decays of the He-like $2\,^1S_0$ state and the line is dominated by $M1$ decays of the
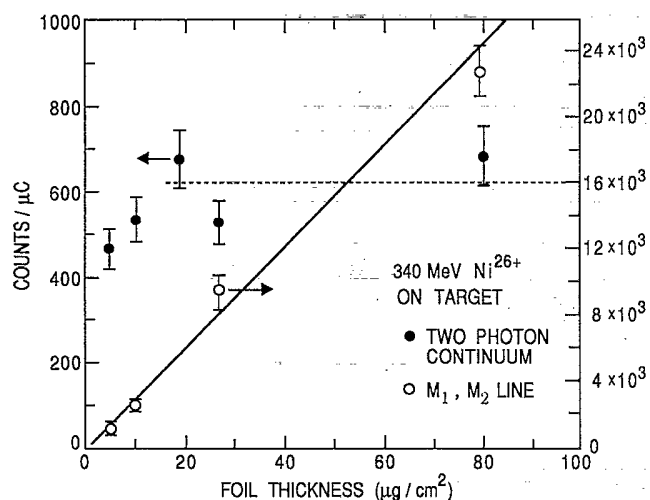

FIG. 7. Yield of photons as a function of foil thickness for a broad cut on the two-photon continuum (solid circles, left axis) and for the peak near 8 keV (open circles, right axis) with ^{58}Ni^{26+} ions incident on the target. The arrows indicate the scale for the data points.

$2\,^3S_1$ level and $M2$ decays of the $2\,^3P_2$ level. These data show a saturation of the two-photon yield for foil thicknesses of greater than about 20 μg/cm^2. On the other hand, the intensity of the $M1,M2$ line shows a linear increase as a function of the foil thickness up to 80 μg/cm^2. Evidently, the $2\,^1S_0$ state has a higher probability of being destroyed within the foil than the $2\,^3S_1$ or $2\,^3P_2$ states which dominate the $M1,M2$ line. In the Appendixes we discuss Stark mixing in the foil as a possible destruction mechanism that could account for this.

For the coincidence measurement of the $2\,^1S_0$ lifetime in He-like Ni, we chose a thin target (12 μg/cm^2) which gave a yield near the plateau of Fig. 7. This choice minimized the singles rate (dominated by the 7.8-keV line) and reduced rate-dependent effects such as pileup, dead time, and accidental coincidences. From the quenching model, a similar dependence of the rate on foil thickness was expected for the $2\,^2S_{1/2}$ state in H-like Ni, and so the 12-μg/cm^2 foil was also used in this case.

C. Two-photon decays

We now consider the two-photon coincidence data used to determine the lifetimes of the H-like $2\,^2S_{1/2}$ state and the He-like $2\,^1S_0$ state. These data were broken into four groups of runs as shown in Table II. Groups 1 and 3, which were done with He-like nickel incident on the target, provided a measurement of the lifetime of the He-like $2\,^1S_0$ state. Groups 2 and 4 were done with bare nickel ions incident on the target and were used to determine the lifetime of the H-like $2\,^2S_{1/2}$ state. In this section, we present details of the analysis of the H-like two-photon data. The analysis for the measurement of the lifetime of the He-like $2\,^1S_0$ state is similar and any differences will be discussed where applicable.

1. Coincidence data

Figure 8 shows a typical time-difference spectrum for detectors 1 and 3. The fast timing signal from detector 1 starts the time-to-amplitude converter and it is stopped by the timing signal from detector 3. The stop is delayed by about 200 ns so the prompt coincidences are shifted by this amount. The random coincidences are evident on either side of the prompt peak. The periodic structure in the random coincidence region is due to the 12.125-MHz pulse structure of the linear accelerator (linac). In order to correct for accidental coincidences, we analyze the data in two windows corresponding to the prompt and random regions of the time-difference spectra. These windows are chosen symmetrically relative to the linac time structure to eliminate any possible error this structure would cause in the subtraction of randoms. The inset of Fig. 8 shows the detector 1–detector 3 time difference spectrum with a requirement that the energy signal from each detector lies within the two-photon continuum. This cut gives a much improved ratio of true to random coincidences. The timing resolution of the Si(Li) detectors varied with the energy of the x rays, being about 20 ns for coincidences between two 8-keV photons but degrading to about 70 ns for typical two-photon coin-

TABLE II. Groups of runs used for the two-photon lifetime measurements.

Group	Incident ion	Beam energy (MeV)	Beam velocity (cm/s)	Carbon target (μg/cm^2)
1	^{58}Ni^{26+}	376	3.5×10^9	12
2	^{58}Ni^{28+}	670	4.7×10^9	12
3	^{58}Ni^{26+}	664	4.7×10^9	12
4	^{58}Ni^{28+}	664	4.7×10^9	12

cidences. Since the linac beam pulses are separated by 82 ns, coincidences between two low-energy x rays do not resolve the pulses and give rise to background of randoms between pulses (see Fig. 8).

Figure 9 shows the correlation between the energies measured by detectors 1 and 3 for "prompt" [Fig. 9(a)] and random [Fig. 9(b)] coincidence events. These data were taken with fully stripped Ni^{28+} on target. Figures 9(a) and 9(b) each correspond to the same number of channels of the time-difference spectrum. In each of these figures, there is a large peak from events in which each detector records an energy of about 8 keV. Since the intensity of this peak is the same in both the prompt and the random cases, this corresponds to accidental coincidences. There are also ridges parallel to the axes which are accidental coincidences between the 8-keV peak and the two-photon continuum. The two-photon coincidences form the diagonal ridge in Fig. 9(a), which corresponds to a sum energy of 8.1 keV. This figure illustrates the excellent isolation of the two-photon coincidences from accidental coincidences. The paucity of remaining accidental coincidences in the two-photon region can be seen in the corresponding diagonal area of Fig. 9(b). These events are subtracted from the prompt coincidences to obtain the true coincidences.

Figure 10 shows sum-energy spectra for prompt and random coincidences between detectors 1 and 3 for fully stripped Ni on target. These spectra are used in the determination of the lifetimes of the two-photon emitting states. We first subtract the random spectra from the prompt spectra to obtain true coincidence spectra for each detector combination. We fit these spectra to two Gaussian functions in the region of the two-photon peak to obtain the H-like and He-like contributions. The fit to these data (Ni^{28+} on target) yields mostly H-like two-photon decays, but there is also a small contribution from He-like two-photon decays, which is 10% at the closest foil position. The fits to the data with Ni^{26+} on target show that the sum-energy peak in this case is almost entirely due to He-like two-photon decays with a negligible contribution from H-like two-photon decays.

The intensities determined by fits to the sum-energy lines at each foil position are normalized by multiplying by the factor
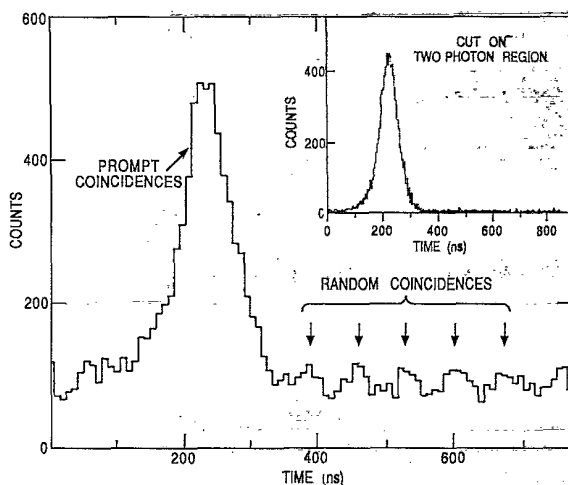

(a)

FIG. 8. Spectrum of time differences between fast timing signals from detectors 1 and 3 for coincidence events. The inset is the time-difference spectrum with a requirement that each photon comes from the two-photon continuum region. These data were taken with 664-MeV ^{58}Ni^{28+} ions incident on the target.

(b)

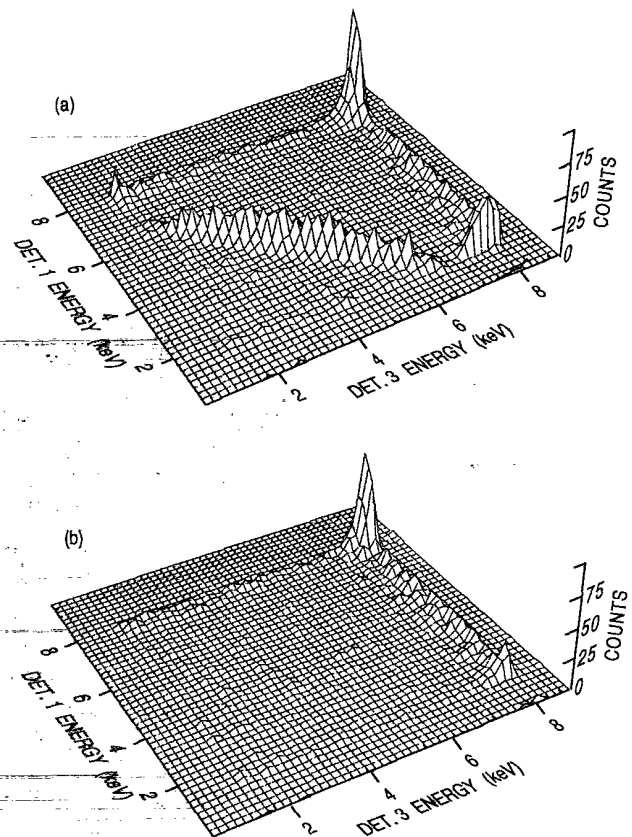FIG. 9. Correlation between the energies measured by detector 1 (left axis) and detector 3 (right axis) for coincident events with 664-MeV ^{58}Ni^{28+} ions incident on the target. (a) "Prompt" coincidences and (b) random coincidences.
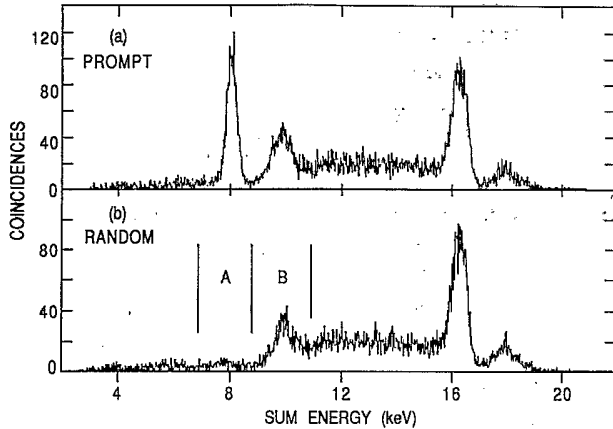
FIG. 10. Sum-energy spectra for (a) prompt and (b) random coincidences.

$$\eta_i = \frac{\frac{1}{n}\sum_n Y_n}{Y_i} \; , \qquad\qquad (33)$$

where Y_i is the normalization count at foil position i and the sum is carried over all motor positions. A typical normalization spectrum is shown in Fig. 11. The inset shows the intensity measured by the normalization detector as a function of motor position. The normalization is fairly constant and so the correction is small. This result indicates that any variations in foil properties were well averaged by our procedure of frequently cycling through the foil positions in measuring the decay curves.

After applying corrections for pileup and cascades, each of the four groups of two-photon coincidence data are fit to a single exponential determining two parameters corresponding to the lifetime and the intensity of the two-photon decay. Excellent fits are obtained for each of the groups. Figures 12(a) and 12(b) show the fit and re-

FIG. 12. (a) Decay curve from coincidence data of group 4. The solid line is a fit to the data. (b) The residuals of the fit.

siduals for the H-like data of group 4. Similar fits are obtained for the other groups. The results of the fits are given in Table III, where we also give a breakdown of the corrections and uncertainties that contribute to the result for the data of group 2.

2. Cascade correction

Cascades through high-lying p states could repopulate the $2\,^1S_0$ and $2\,^2S_{1/2}$ levels downbeam of the foil and dis-
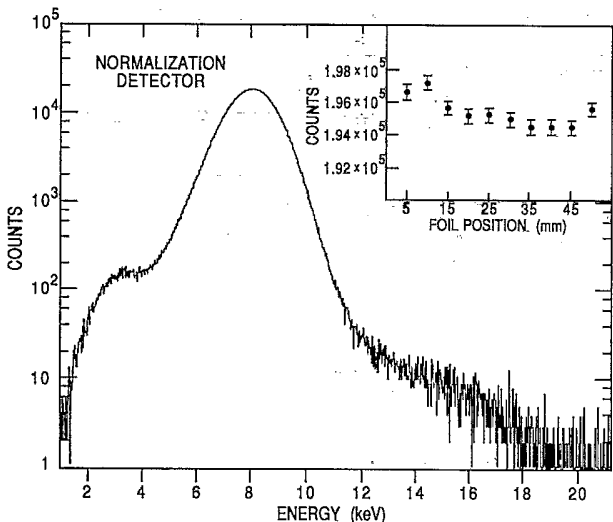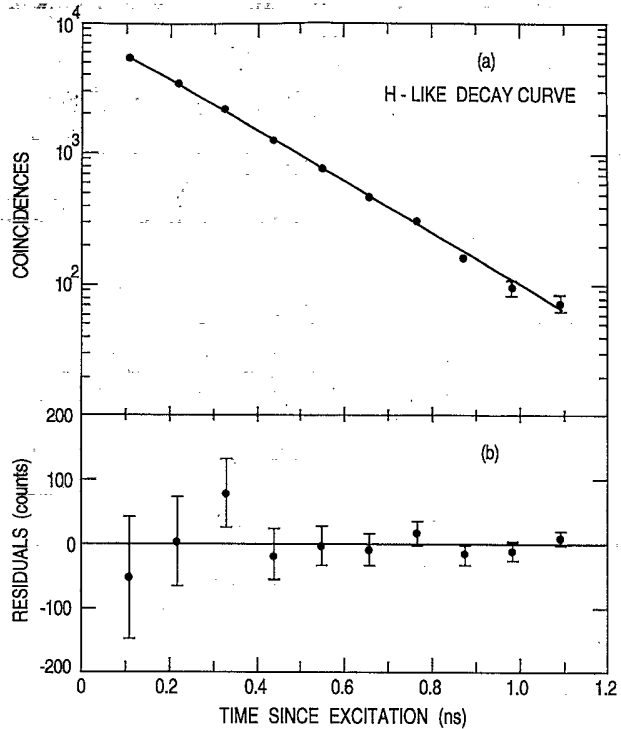
FIG. 11. Spectrum taken with the normalization detector. The inset shows the counts in the peak of the normalization spectrum plotted as a function of the foil position for the data of group 2.

TABLE III. Results and uncertainties for the two-photon lifetime measurements.

Description	Lifetime (ps)
H-like fit result (group 2)	216.5 ± 2.3
Pileup[a]	(-13.2 ± 0.8)
He-like component[a]	$(+1.7\pm0.6)$
Normalization[a]	$(+1.3\pm0.2)$
Random coincidences[a]	$(+5.2\pm0.7)$
Time dilation[a]	(-2.58)
Cascades to $2\,^2S_{1/2}$[a]	-0.41 ± 0.30
Velocity and position measurement error[a]	±0.65
Result H-like group 2	216.1 ± 2.4
Result H-like group 4	218.2 ± 2.6
Final result H-like $2\,^2S_{1/2}$ state	217.1 ± 1.8
Result He-like group 1	155.3 ± 2.0
Result He-like group 3	157.3 ± 2.6
Final result He-like $2\,^1S_0$ state	156.1 ± 1.6

[a]The error budget is given only for the H-like group 2 data. The numbers for the other groups are similar. The corrections and errors in parentheses are already included in the fit result given in the first line.

tort the decay curves. Our method of handling this potential systematic effect is based on the fact that any cascade that repopulates $2\,^1S_0$ or $2\,^2S_{1/2}$ will have a branch to the ground state with a known branching ratio. The ground-state decays $np \rightarrow 1s$ contribute to the Si(Li) spectrum in the region above 8 keV.

The cascade decays can be described using the relations developed in Sec. IV. First consider the decays $3p \rightarrow 1s$. In the notation of Sec. IV, the rate of detection of the decay photons is given by

$$N_i^{3p1s}(z_d) = \epsilon_i(E_{3p1s})$$
$$\times \int_0^\infty R_{3p1s}(z)dz \frac{\Omega_i(z-z_d)}{4\pi}$$
$$\times A_i^{3p1s}(z-z_d) . \qquad (34)$$

The function $R_{3p1s}(z)$ typically does not vary rapidly over the region viewed by the detectors (about 5 mm), so we pull it out of the integral and solve Eq. (34) for $R_{3p1s}(zd)$ at a number of discrete points z_d in terms of the measured rates $N_{3p1s}(z_d)$. The ratio of the transition probabilities for the decay of the $3p$ state,

$$b_{3p} = \frac{w_{3p-2s}}{w_{3p-1s}} , \qquad (35)$$

is known theoretically [46], so we can calculate the rate of $3p \rightarrow 2s$ decays $R_{3p2s}(z)$ in terms of the known quantities $R_{3p1s}(z)$:

$$R_{3p2s}(z) = b_{3p}R_{3p1s}(z) . \qquad (36)$$

Using $R_{3p2s}(z)$, we then calculate the rate of two-photon decays at position z for ions populated by cascade transitions in the region between the foil and z. This is given by

$$R_{2E1}^{casc}(z)dz = \frac{dz}{L_{2s}} \int_{z_0}^z R_{3p-2s}(z')e^{(z-z')/L_{2s}}dz' \qquad (37)$$

where

$$L_{2s} = \frac{\omega_{2s}}{v} \qquad (38)$$

is the decay length for the $2s$ ion and v is the velocity of the ions. Equation (37) accounts for both the accumulation of $2s$ ions from cascades and the decay of these states after formation. Using $R_{2E1}^{casc}(z)$ determined from Eq. (37), and substituting into Eq. (26) or (27), we calculate the rate for the detection of singles or coincidence two-photon events arising from cascades from higher-lying states. These results are used to correct the singles and coincidence data at each foil position.

In applying this procedure to the H-like two-photon decay measurement, the intensities for the transitions $np \rightarrow 1s$ are determined by fitting the region above the $M1$ line. These results are then used to determine corrections to the data at each foil position. The corrections are less than 0.1% at the closest foil position but rise to about 1% at the most distant foil positions. In Table III, we indicate the effect of the cascade correction on the lifetime measurement for the data of group 2. This was

determined by comparing fits to the data before and after the corrections were made.

3. Stark and collisional quenching

If the metastable states are destroyed by electric field quenching or by collisional deexcitation, this will also distort the decay curve and cause a systematic error in the lifetime measurement. Although low-Z H-like ions are very sensitive to quenching by stray electric fields, the sensitivity to electric fields is much smaller for highly charged ions. The Stark effect causes a mixing of the $2\,^2S_{1/2}$ state with the $2\,^2P_{1/2}$ state. For small perturbations the $2\,^2S_{1/2}$ becomes

$$\psi'_{2\,^2S_{1/2}} = \psi_{2\,^2S_{1/2}} + \epsilon\psi_{2\,^2P_{1/2}} \qquad (39)$$

where ϵ is the mixing parameter given by

$$\epsilon = \frac{\langle 2\,^2P_{1/2}|\sqrt{3}ea_0\mathbf{E}\cdot\mathbf{r}|2\,^2S_{1/2}\rangle}{\Delta E - i\Gamma_{2p}/2} . \qquad (40)$$

Here $\mathbf{E}$ is the electric field, ΔE is the Lamb shift, and Γ_{2p} is the width of the $2p$ level. Evaluating the matrix element and keeping track of the dependence on the nuclear charge Z, we find

$$|\epsilon| \approx \frac{E}{500Z^5} , \qquad (41)$$

where E is expressed in V/cm. The decay rate for the perturbed $2\,^2S_{1/2}$ is given by

$$\omega'_{2\,^2S_{1/2}} = \omega_{2\,^2S_{1/2}} + |\epsilon|^2\omega_{2\,^2P_{1/2}} . \qquad (42)$$

Evaluating this expression for nickel, we find that a field of about 60 MV/cm is required for the second term to be 1% of the decay rate. This is much larger than any fields acting on the metastable ions so Stark mixing is a negligible effect in our experiment.

Collisions with background gas can also quench the metastable ions. In Appendix B, we present an estimate of the cross section for collisional quenching which is found to be less than 10^{-17} cm^2. Our target chamber vacuum was better than 10^{-7} Torr during the runs, so the mean free path for destruction of metastable ions is greater than 100 km and this systematic effect is also negligible.

4. Detector cross talk

If an 8-keV photon undergoes a Compton scattering in one detector and the scattered photon is detected by a second detector, this gives a true coincidence event with the proper sum energy and thus mimics a two-photon decay. Such a "cross-talk" event is most likely for coincidences between detectors 1 and 3 because of the geometrical arrangement of the detectors (see Fig. 3). This process would be most prominent at the farthest foil position where the ratio of the intensities of the 8-keV line to the two-photon decays is greatest. For our H-like data, the 8-keV line at the farthest foil position arises mostly from cascades through the $2p$ states, and it has an intensity of about 8 times the two-photon intensity at this foil posi-

tion. The fraction of interactions of an 8-keV x ray that involve Compton scattering is 1.5×10^{-3} for silicon [47]. Taking into account the geometry of detectors 1 and 3, but assuming the same efficiency for the two processes, the rates for Compton scattering coincidences would be 0.3% of the coincidence rate from two-photon decay. The actual rate is smaller than this because the average energy imparted [47] to the Si electrons in Compton scattering is about 120 eV, which is well below our detection thresholds. In addition, some of the scattered photons will be absorbed in the silicon or absorbing layers of the first detector.

In a related process, if the characteristic Si x ray emitted following photoelectric ejection of an electron by an 8-keV photon escapes to the opposite detector, this also gives rise to a coincidence with the proper sum energy. Tests using a ^{65}Zn source which emits an 8-keV x ray indicate the probability of escape of a Si K x ray is about 0.2%. Using the count rate for the 8-keV line and accounting for solid angles and detection efficiencies, we estimate the coincidence rate at the farthest foil position for a Si-escape event is about 0.1% of the two-photon coincidence rate.

Our results indicate that the ratio of cross-talk events to two-photon events gets smaller as the foil is brought closer to the detectors, and we find that cross talk contributes a negligible error to both the H-like and the He-like results. Back-to-back Compton scattering becomes more important for measurements of two-photon decays in higher-Z ions. For example, at 30 keV, 11% of the photons Compton scatter depositing an average energy of 1.6 keV. On the other hand, the Si escape probability becomes lower for higher-energy photons since the interactions occur deeper in the crystal.

D. Yrast cascades

The most striking difference between the prompt and random sum-energy spectra (detector 1+detector 3) of Fig. 10 is the absence of the two-photon coincidence peak (region A) in the spectrum of random coincidences; but there is also a difference in region B of the two spectra. Although there are peaks in both spectra, there are more counts in this region in the prompt spectrum, so some of these must be true coincidences. In this section, we examine the singles spectra corresponding to regions A and B of Fig. 10 in order to identify the origin of the true coincidences.

In Fig. 13 we show energy spectra from detector 1 for coincidences associated with region A of the sum-energy spectra. Figures 13(a) and 13(b) correspond to the prompt and random regions of the time spectrum. Figure 13(c) is the difference of these two spectra and corresponds to the true coincidences. The true coincidences exhibit the continuum expected for two-photon decays. The low-energy cutoff arises from absorption of low-energy x rays and the discriminator setting in the fast-timing electronics for detector 1. There is also a high-energy cutoff. Since the sum of the energies in detectors 1 and 3 is a constant, the high-energy region in detector 1 corresponds to the low-energy region of detector 3. So
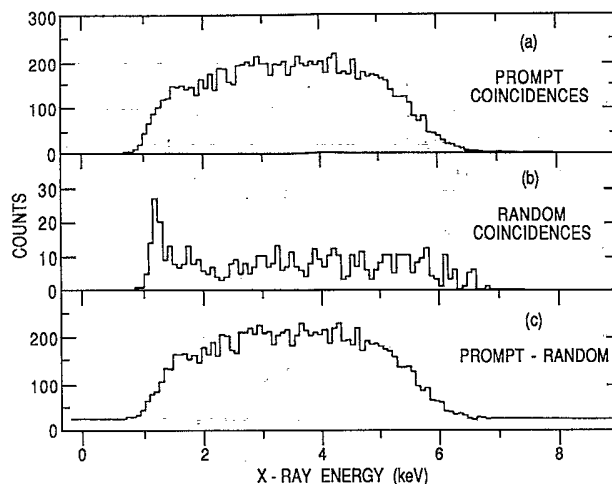

FIG. 13. Energy spectra from detector 1 for coincidence events that fall into region A of the sum-energy spectrum [see Fig. 10(b)]. (a) Prompt coincidences, (b) random coincidences, and (c) the difference between spectra (a) and (b) with an offset of 20 counts.

the high-energy cutoff in Fig. 13 is governed by absorption and pulse height discrimination in detector 3.

A similar analysis of the spectra in detector 1 corresponding to region B of Fig. 10 provides a clear indication that there are true coincidences associated with this sum energy. In Fig. 14 we show energy spectra in detector 1 for events with sum energy in region B. The spectrum of true coincidences [Fig. 14(c)] is dominated by two peaks. One, near 8 keV, corresponds to H-like transitions from $n = 2$ to 1, while the other corresponds H-like $n = 3$ to 2 transitions. The presence of these two peaks suggests that these events are yrast cascades $3d \rightarrow 2p \rightarrow 1s$. The asymmetry between the low- and high-energy peaks appears because detector 1 is more sensitive to low-energy photons. The corresponding spectra of detector 3 show a larger peak near 8 keV.

Without the coincidence technique it is difficult to identify yrast events because the resolution of the Si(Li)
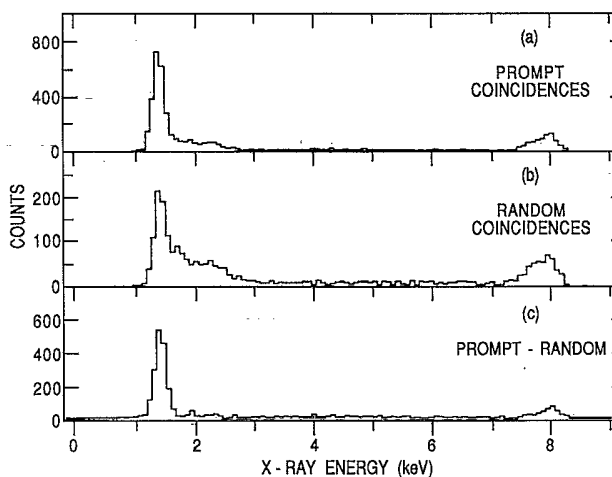

FIG. 14. Same as Fig. 13 for events falling into region B of the sum-energy spectrum [see Fig. 10(b)].

detectors is not sufficient to distinguish the $3d \rightarrow 2p$ decays from other H-like $n = 3 \rightarrow n = 2$ decays. The $3d \rightarrow 2p$ region is further complicated by unresolved He-like and Li-like lines. The clear identification of the coincidence from yrast cascades allows a study of the time dependence of these decays. Figure 15 is a log-log plot of the decay curve for yrast coincidences together with a fit to a straight line showing that the data are well represented by a power law

$$I(t) = I_0 t^{-\lambda_y} \qquad (43)$$

with $\lambda_y = 1.26(3)$. A power-law dependence for cascade events has been well established experimentally [48–50]. It is sometimes referred to as the $t^{-3/2}$ law, but our result differs somewhat from an exact $\frac{3}{2}$ power. Theoretical treatments [51] establish the law based on the initial population of a large number of different Rydberg levels. These treatments give an exact $\frac{3}{2}$ power only with a special choice of initial population conditions, not necessarily applying to our experimental system.

E. He-like triplet states

In Fig. 5, which shows data taken with bare Ni^{28+} on target, the single-photon line near 8 keV is a blend of H-like and He-like transitions. However, we are able to obtain a clean separation between these two species by fitting the region to two Gaussian functions. By contrast, in Fig. 6, which shows data taken with Ni^{26+} incident on the target, there is very little H-like intensity and the peak at 7.8 keV consists mostly of decays from the $n = 2$ levels of He-like Ni^{26+}. A study of the energy levels in Fig. 1 shows that the Si(Li) detector energy resolution of 200 eV is too large to resolve the decays of the different He-like sublevels in $n = 2$. Apart from the two-photon decays of the $2\,^1S_0$ level which form a continuum below the peak, the only means we have of distinguishing the different levels in our experiment is by their lifetimes. Fortunately, there is a very broad range of lifetimes in-

volved. The $2\,^1P_1$ and $2\,^3P_1$ levels are so short lived that they decay very near the foil and apart from repopulation from cascades, these states decay away well before the ions reach the field of view of the detectors. Since the $2\,^3P_0$ and $2\,^3S_1$ levels are comparatively long lived, the $2\,^3P_2$ level is separated well enough in lifetime from the other levels to allow a measurement of its lifetime. The result of this measurement was reported earlier [3]. The decay curve from the 7.8-keV peak was fitted to two exponentials and a constant background. This fit determined the lifetime to be

$$\tau_{2\,^3P_2} = 70(3) \text{ ps} . \qquad (44)$$

It is difficult to measure the lifetimes of the $2\,^3P_0$ and $2\,^3S_1$ levels in He-like nickel because the two lifetimes are similar and the sensitivity of a fit of the decay curve to the individual lifetimes is small. One way to handle this problem is to study the decay in ^{61}Ni. In this isotope, the $2\,^3P_0$ level is quenched to the ground state by the hyperfine interaction and the lifetime is reduced from 2.5 ns to 450 ps. This allows a separation between $2\,^3P_0$ and $2\,^3S_1$ in the decay curve. Although the three component decay curve involving the $2\,^3P_2$, $2\,^3P_0$, and $2\,^3S_1$ states is complicated, we are able to fit it to three exponentials by comparing data from the two isotopes ^{58}Ni and ^{61}Ni. The method used is to first fit the ^{58}Ni data to obtain an experimental lifetime for the $2\,^3P_2$ state and then to fix this in the fit to the ^{61}Ni data. Although the $2\,^3P_2$ state is also affected by hyperfine quenching, the change in its lifetime is small enough to be ignored at our present level of experimental precision. We have used this procedure to determine the lifetime of the $2\,^3P_0$ level in ^{61}Ni [3]. Since we do not have sufficient foil movement to make a reliable determination of the $2\,^3S_1$ lifetime, we fix this at the theoretical value. This lifetime had been measured in other high-Z ions [52,53] and the results of these measurements all agreed with theory. The result for the $2\,^3P_0$ lifetime is

$$\tau_{2\,^3P_0}^{61Ni} = 470(50) \text{ ps} , \qquad (45)$$

which agrees with all theoretical calculations presented in Table IV. We also use this result, together with the theoretical values for the hyperfine matrix elements and the unquenched lifetimes, to determine the $2\,^3P_0 - 2\,^3P_1$ energy splitting with the result [3]

$$|\Delta E_{0-1}| = 2.33(15) \text{ eV} . \qquad (46)$$

In a recent publication [54], the theoretical and experi-

TABLE IV. Theoretical and experimental results for the lifetime of the $2\,^3P_0$ level in He-like $^{61}Ni^{26+}$.

Experiment (ps)	Theory (ps)
470±50[a]	443[b]
	464[c]
	450[d]

[a]Reference [3].
[b]Reference [39]
[c]Reference [73].
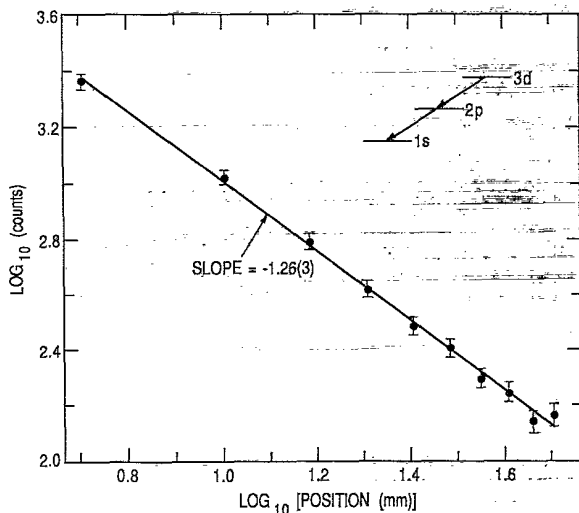[d]Reference [74].

FIG. 15. Log-log plot of counts vs foil position for coincidences associated with cascades $3d \rightarrow 2p \rightarrow 1s$.

mental results for all the fine-structure splittings in He-like ions were compared. Although the result in Eq. (46) agrees with the benchmark calculations of Drake [55], more precise measurements of $2\,^3P$ state fine structures indicate a systematic difference between theory and experiment for the $2\,^3P_0$ state energy. Recent relativistic many-body perturbation-theory calculations by Johnson and Sapirstein [56] are in agreement with these precise measurements.

VI. COMPARISON OF THEORY AND EXPERIMENT

A. H-like $2\,^2S_{1/2}$ state

In Table V, we list the theoretical and experimental results for the lifetimes of the $2\,^2S_{1/2}$ level in one-electron ions. Measurements have been made over a range of nuclear charge from 1 to 36. A precision of about 1% has been achieved for He$^+$ [57,58], Ar^{17+} [59], and Ni^{27+} [2]. Lower precision measurements have been made in O^{7+}, F^{8+} [60], S^{15+} [61], and Kr^{35+} [42]. The Ar^{17+} experiment was the first to be sensitive to the contribution of the magnetic dipole amplitude to the total decay rate. The Ni^{27+} measurement was the first to be sensitive to the relativistic corrections of the two-photon decay rate, and the Kr^{35+} experiment provided the first direct measurement of the branching ratio for the $M1$ decay mode. Figure 16 is a comparison of experiment and theory for the $2\,^2S_{1/2}$ lifetime $(Z > 1)$ illustrating the good agreement for the measurements. The dashed line shows the nonrelativistic theoretical results. For low Z, the nonrelativistic result gives a shorter lifetime, but there is a crossover at about $Z = 37$, and for higher Z the nonrelativistic results gives a longer lifetime. This behavior arises because the two-photon decay dominates at low Z while the $M1$ decay dominates at high Z and the two
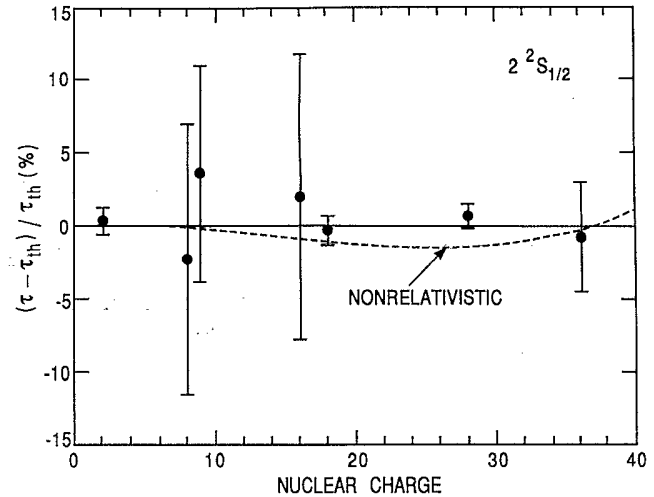

FIG. 16. Difference between the relativistic theory (τ_{th}) (Refs. [12] and [14]) and experiment for the lifetime of the $2\,^2S_{1/2}$ level in one-electron ions as a function of nuclear charge, expressed as a percentage of the theoretical value. The dashed line is the difference between the nonrelativistic and the relativistic theory for the lifetime.

modes are effected in opposite ways by the relativistic corrections.

Our result can place a crude limit on parity mixing in a one-electron atom. The weak interaction mixes the $2s$ and $2p$ levels so that the perturbed $2s$ state is

$$\psi'_{2\,^2S_{1/2}} = \psi_{2\,^2S_{1/2}} + \delta_w \psi_{2\,^2P_{1/2}} \tag{47}$$

and the decay rate is

$$\omega'_{2\,^2S_{1/2}} = \omega_{2\,^2S_{1/2}} + |\delta_w|^2 \omega_{2\,^2P_{1/2}} \,. \tag{48}$$

From the agreement between experiment and theory for

TABLE V. Experimental and theoretical lifetimes and branching ratios for the $2\,^2S_{1/2}$ level in H-like ions.

Z	Experiment (s)	Theory[a] (s)	nr Theory[a] (s)	$M1$ branching ratio (Theory)[a]
1	0.67 ± 0.29[b]	0.121 58	0.121 59	3.033×10^{-7}
2	$(1.922\pm0.082)\times10^{-3}$[c]	$1.898\,2\times10^{-3}$	$1.897\,9\times10^{-3}$	4.853×10^{-6}
	$(2.04+0.81-0.34)\times10^{-3}$[d]			
	$(1.905\pm0.018)\times10^{-3}$[e]			
8	$(453\pm43)\times10^{-9}$[f]	463.55×10^{-9}	462.55×10^{-9}	1.247×10^{-3}
9	$(237\pm17)\times10^{-9}$[f]	228.62×10^{-9}	228.00×10^{-9}	1.996×10^{-3}
16	$(7.3\pm0.7)\times10^{-9}$[g]	$7.153\,0\times10^{-9}$	$7.094\,7\times10^{-9}$	0.019 93
18	$(3.54\pm0.25)\times10^{-9}$[g]	$3.494\,1\times10^{-9}$	$3.459\,4\times10^{-9}$	0.031 73
	$(3.487\pm0.036)\times10^{-9}$[h]			
28	$(217.1\pm1.8)\times10^{-12}$[i]	215.45×10^{-12}	212.34×10^{-12}	0.166 7
36	$(36.8\pm1.4)\times10^{-12}$[j]	37.008×10^{-12}	26.982×10^{-12}	0.364 3

[a]References [14,12]. Branching ratios from Ref. [14].   [f]Reference [60].
[b]Reference [75].   [g]Reference [61].
[c]Reference [57].   [h]Reference [59].
[d]Reference [76].   [i]Reference [2].
[e]Reference [58].   [j]Reference [42].

our measurement, we can place a limit on the mixing parameter

$$|\delta_w| < 3 \times 10^{-4} . \tag{49}$$

This is much larger than the mixing expected based on the standard model [62]:

$$|\delta_w|_{th} \sim 7 \times 10^{-10} . \tag{50}$$

A lifetime experiment does not provide a sensitive test of parity nonconservation because of the quadratic dependence of the decay rate on the mixing parameter indicated in Eq. (48). An interference effect which is linear in the mixing parameter [62,63] can provide a more sensitive search.

We can also place a limit on Feinberg's coupling constant λ for the anapole or pseudocharge interaction [64]. The error in our measurement of the H-like $2\,{}^2S_{1/2}$ lifetime places a limit on this interaction of

$$|\lambda| < 2.2 \times 10^{-5} . \tag{51}$$

Again, more stringent limits can be obtained from atomic parity violation experiments.

B. He-like $2\,{}^1S_0$ state

A comparison of theory and experiment for the lifetime of the $2\,{}^1S_0$ level in He-like ions is given in Table VI. The lifetime has been measured to about 1% in Ni^{26+}, Br^{33+}, and Kr^{34+}, and less precisely in He, Li^+, and Ar^{16+}. The nickel, bromine, and krypton results are the only measurements that test the relativistic corrections to the theory. In this case the relativistic result is based on a screened hydrogenic calculation, and the theoretical error is an estimate of how much this could differ from a fully relativistic calculation. A goal for future experiments is to obtain a precision better than that of the current theoretical error. The coincidence technique used here appears to be the best approach, since the systematic errors are well under control. The main limitation of this technique is the statistical uncertainty. In future experiments, the coincidence rate could be improved by increasing the number of independent Si(Li) crystals.

An array of crystals on a single cryostat could be used for this purpose. Two such detectors, each equipped with five crystals, would improve the coincidence rate by a factor of 25, which would give an improvement of a factor of 5 in the statistical accuracy. Another factor that could lead to an improved test of relativistic corrections would be to do the measurement in a higher-Z ion since the relativistic corrections increase with Z. Recently an experiment using Br $(Z=35)$ which achieved a precision of about 1% using the coincidence technique described in this paper has been reported [65]. In addition to an increased sensitivity to relativistic effects, the higher Z ions also have a better separation of the sum-energy peaks for the H-like and He-like two-photon decays. This would reduce the error associated with the fits to the sum-energy spectra.

C. He-like $2\,{}^3P_2$ state

In Table VII we present the existing measurements of the lifetime of the $2\,{}^3P_2$ level in He-like ions together with the theoretical predictions. All of the measurements agree with theory to within the experimental error. For the odd mass (A) isotopes, there is an additional contribution to the decay rate due to hyperfine quenching. This contribution is less than the experimental error except for vanadium $(Z=23, A=51)$. In this isotope, Gould, Marrus, and Mohr [31] were able to observe the effect of hyperfine quenching. The nickel measurement is the highest-Z measurement of the lifetime of the $2\,{}^3P_2$ level. An improved measurement of this lifetime would be desirable, since this is one of the few cases of an $M2$ transition in atomic physics. A precise measurement at higher Z would be ideal, since the branching ratio for the $M2$ decay is larger and such a measurement would be more sensitive to relativistic effects. The difficulty with a high-Z measurement is that the lifetime of the $2\,{}^3P_2$ level becomes very short as Z increases and one must use highly collimated detectors to view the beam within a fraction of a mm of the foil without viewing the foil. It is a challenge for the future to extend these lifetime measurements to shorter decay lengths.

TABLE VI. Experimental and theoretical results for the lifetime of the $2\,{}^1S_0$ level He-like atoms.

Z	Experiment (s)	Theory[a] (s)	nr Theory[a] (s)
2	$(38\pm8)\times10^{-3}$ [b] $(19.7\pm1.0)\times10^{-3}$ [c]	$(19.630\pm0.028)\times10^{-3}$	19.600×10^{-3}
3	$(503\pm26)\times10^{-6}$ [d]	$(515.85\pm0.47)\times10^{-3}$	515.27×10^{-3}
18	$(2.3\pm0.3)\times10^{-9}$ [e] $(2.32\pm0.20)\times10^{-9}$ [f]	$(2.3725\pm0.0056)\times10^{-9}$	2.3432×10^{-9}
28	$(150\pm16)\times10^{-12}$ [g] $(156.1\pm1.6)\times10^{-12}$ [h]	$(154.28\pm0.50)\times10^{-12}$	150.00×10^{-12}
35	$(39.32\pm0.32)\times10^{-12}$ [i]	$(39.63\pm0.16)\times10^{-12}$	37.972×10^{-12}
36	$(34.08\pm0.34)\times10^{-12}$ [j]	$(33.41\pm0.13)\times10^{-12}$	31.943×10^{-12}

[a]Reference [12].
[b]Reference [77].
[c]Reference [78].
[d]Reference [79].
[e]Reference [61].
[f]Reference [59].
[g]Reference [1].
[h]Reference [2].
[i]Reference [65].
[j]Reference [80].

TABLE VII. Experimental and theoretical lifetimes for the $2\,^3P_2$ level in He-like ions.

Z	A	Experiment (s)	Theory[a] (s)
9	19	$(10\pm1)\times10^{-9}$ [b]	10.3×10^{-9}
		$(10.44\pm0.15)\times10^{-9}$ [c]	
13	27	$(5.4\pm0.2)\times10^{-9}$ [d]	5.11×10^{-9}
15	31	$(3.4\pm0.3)\times10^{-9}$ [e]	3.33×10^{-9}
16	32	$(2.5\pm0.2)\times10^{-9}$ [f]	2.60×10^{-9}
17	35	$(1.86\pm0.1)\times10^{-9}$ [g]	1.98×10^{-9}
18	40	$(1.7\pm0.3)\times10^{-9}$ [h]	1.48×10^{-9}
		$(1.62\pm0.08)\times10^{-9}$ [i]	
22	48	$(440\pm30)\times10^{-12}$ [i]	422×10^{-12}
23	51	j	$(202-313)\times10^{-12}$ [j]
26	56	$(112\pm13)\times10^{-12}$ [k]	125×10^{-12}
28	58	$(70\pm3)\times10^{-12}$ [l]	70.6×10^{-12}

[a]References [32,34].
[b]Reference [81].
[c]Reference [82].
[d]Reference [83].
[e]Reference [84].
[f]Reference [85].
[g]Reference [86].
[h]Reference [61].
[i]Reference [87].
[j]Decay curve was a composite of several hyperfine transitions. See Refs. [31,4].
[k]References [31,4].
[l]Reference [3].

APPENDIX A: QUENCHING BY THE STOPPING-POWER FIELD IN THE FOIL

A 664-MeV Ni^{27+} ion interacting with a carbon foil "sees" an electric field of about 2×10^9 V/cm that slows the ion as it traverses the foil [66]. The Stark interaction energy for the mixing of the H-like $2\,^2S_{1/2}$ and $2\,^2P_{1/2}$ levels in this field is about 1 eV [46], which is larger than the 0.77-eV energy separation (Lamb shift) between these states so they are strongly mixed. In the limit of complete mixing, these two states each have a lifetime of 5.2 fs [46] and significant quenching of the 2s state will occur in the foil. For the He-like $2\,^1S_0$ state, the matrix element for mixing with the $2\,^1P_1$ state is also about 1 eV, but the $2\,^1S_0-2\,^1P_1$ splitting is 39 eV in He-like Ni^{26+}, so the level is less strongly perturbed by this electric field. Nevertheless, strong mixing of the $2\,^1S_0$ level may occur from collisions with foil nuclei, as discussed in Appendix C.

APPENDIX B: QUENCHING FROM COLLISIONS WITH BACKGROUND GAS

The problem of quenching of metastable hydrogen from collisions with charged particles in a plasma has been treated by Purcell [67], Goss and Field [68], Percival and Richards [69], and Seaton [70,71]. We will generalize Purcell's treatment to collisions of charged particles with high-Z H-like ions in the $2\,^2S_{1/2}$. This result will then be used to obtain an upper limit to the destruction cross sections for this state from collisions with the background gas.

The generalization to Purcell's Eq. (6) is

$$w' = \frac{12e^4a_0^2Z_t^2}{\hbar^2v^2b^2Z_i^2} \qquad \text{(B1)}$$

This gives the probability w' that a H-like ion of nuclear charge Z_i, initially in the $2\,^2S_{1/2}$ level, will make a transition to the $2\,^2P_{1/2}$ level after a collision with a particle of charge Z_t at an impact parameter b and velocity v. Equation (B1) is valid for $b\ll v/\omega'$, where ω' is the Lamb shift expressed in circular frequency units. For sufficiently small b, w' could exceed one, so following Wilcox and Lamb [72], we replace Eq. (B1) by

$$w' = \tfrac{1}{3}\sin^2(B/b) , \qquad \text{(B2)}$$

where

$$B^2 = \frac{36Z_t^2\alpha^2a_0^2}{\beta^2Z_i^2} , \qquad \text{(B3)}$$

α is the fine-structure constant, and $\beta=v/c$. Similarly the parameter w'' is defined to be the probability for a transition to the $2\,^2P_{3/2}$ state,

$$w'' = \tfrac{2}{3}\sin^2(B/b) . \qquad \text{(B4)}$$

For collisions of 664-MeV nickel ions with slow gas atoms, $v/\omega'=300$ Å and $v/\omega''=6$ Å. For collisions with neutral gas atoms only impact parameters $b<1$ Å give rise to appreciable quenching and this is well within the region of validity of Eq. (B1). To find an upper limit on the destruction cross section, we neglect shielding by the electrons of the gas atom and consider a collision with the nucleus. The cross section [72] for a transition to the $2\,^2P_{1/2}$ level is

$$\sigma' = 2\pi\int_0^{r_c'} w'(b)\,db , \qquad \text{(B5)}$$

and there is a similar expression for transitions to the $2\,^2P_{3/2}$ state. An approximate formula for the integral [72] is

$$\sigma' = (2\pi/3)B^2[\tfrac{3}{2}-0.577-\ln(B/r_c')] . \qquad \text{(B6)}$$

Taking $r_c'=v/\omega'$ and $r_c''=v/\omega''$, we find $\sigma'\approx3\times10^{-18}$ cm^2 and $\sigma''\approx4\times10^{-18}$ cm^2 for upper limits to the destruction cross sections for collisions with nitrogen ($Z_t=7$). As a more realistic estimate, taking screening into account, we set both r_c' and r_c'' equal to 1 Å, in which case the destruction cross section is $\sigma'+\sigma''\approx4\times10^{-18}$ cm^2. The 2s level will also be mixed with higher-lying np

levels in collisions with charged particles. We used Purcell's theory to estimate the sum of the cross sections for transitions to all other np levels, which was found to be about 1×10^{-18} cm^2. These estimates are the basis for our limits on the effect of metastable quenching on the lifetime measurements discussed in Sec. V C 3.

APPENDIX C: QUENCHING BY COLLISIONS WITH FOIL NUCLEI

We can use the results of Appendix B to estimate metastable destruction in collisions of H-like $2s$ ions with the carbon nuclei of the foil. Assuming the cross section of 4×10^{-18} cm^2 is also approximately valid for collisions with carbon nuclei, the average time between collisions would be 0.5 fs, which is small compared to the unperturbed $2p$ state lifetime of 2.6 fs. The actual lifetime of the $2p$ state will be reduced by charge-changing collisions within the foil, but it is likely that the $2p$ amplitude will not decay completely before another collision. Under these conditions, a better picture might be that the interactions in the foil maintain the ion in a superposition of $2s$ and the $2p$ states (and other levels). Under these conditions, the total amplitude for being in $n = 2$ will decay with a lifetime on the order of the lifetime of the $2p$ state in the foil.

These considerations suggest a mechanism to explain the difference in behavior between the yields of the triplet and singlet He-like states as a function of foil thickness (see Fig. 7). Since the fine-structure separations are similar, the cross sections for $2s \rightarrow 2p$ transitions in He-like ions would be similar to σ'', the cross section for H-like $2\,^2S_{1/2} \rightarrow 2\,^2P_{3/2}$ transitions. From the considerations of Appendix B, we would expect a superposition of $2s$ and $2p$ levels within the foil. To the extent that the singlet and triplet character of these mixtures is preserved, the triplet states would be longer lived, since the $2\,^3P_J$ levels are longer lived (see Fig. 1) than the $2\,^1P_1$ level. The actual interactions within the foil are quite complicated, however, and a more complete analysis would be required to gain a full understanding of the yields of the various states in the foil.

*Permanent address: Department of Physics, Texas A&M University, College Station, TX 77843.

†Permanent address: Weizmann Institute of Science, Rehovot, Israel.

‡Permanent address: AT&T Bell Laboratories, Middletown, NJ 07748.

§Permanent address: Department of Physics, Kansas State University, Manhattan, KS 66506.

[1] R. W. Dunford, H. G. Berry, K. O. Groeneveld, M. Hass, E. Bakke, M. L. A. Raphaelian, A. E. Livingston, and L. J. Curtis, Phys. Rev. A **38**, 5423 (1988).

[2] R. W. Dunford, M. Hass, E. Bakke, H. G. Berry, C. J. Liu, M. L. A. Raphaelian, and L. J. Curtis, Phys. Rev. Lett. **62**, 2809 (1989).

[3] R. W. Dunford, C. J. Liu, J. Last, N. Berrah-Mansour, R. Vondrasek, D. A. Church, and L. J. Curtis, Phys. Rev. A **44**, 764 (1991).

[4] R. Marrus and P. J. Mohr, Adv. At. Mol. Phys. **14**, 181 (1978).

[5] M. Goeppert-Mayer, Ann. Phys. (Leipzig) **9**, 273 (1931).

[6] G. Breit and E. Teller, Astrophys. J. **91**, 215 (1940).

[7] L. Spitzer, Jr. and J. L. Greenstein, Astrophys. J. **114**, 407 (1951).

[8] J. Shapiro and G. Breit, Phys. Rev. **113**, 179 (1959).

[9] B. A. Zon and L. I. Rapoport, Pis'ma Zh. Eksp. Teor. Fiz. **7**, 70 (1968) [JETP Lett. **7**, 52 (1968)].

[10] S. Klarsfeld, Phys. Lett. **30A**, 382 (1969).

[11] S. Klarsfeld, Lett. Nuovo Cimento **1**, 682 (1969).

[12] G. W. F. Drake, Phys. Rev. A **34**, 2871 (1986).

[13] W. R. Johnson, Phys. Rev. Lett. **29**, 1123 (1972).

[14] F. A. Parpia and W. R. Johnson, Phys. Rev. A **26**, 1142 (1982).

[15] S. P. Goldman and G. W. F. Drake, Phys. Rev. A **24**, 183 (1981).

[16] S. P. Goldman, Phys. Rev. A **40**, 1185 (1989).

[17] Z. Fried and A. O. Martin, Nuovo Cimento **29**, 574 (1963).

[18] R. Bacher, Z. Phys. A **315**, 135 (1984).

[19] A. Dalgarno, Mon. Not. R. Astron. Soc. **131**, 311 (1966).

[20] A. Dalgarno and G. A. Victor, Proc. Phys. Soc. London **87**, 371 (1966).

[21] G. A. Victor, Proc. Phys. Soc. London **91**, 825 (1967).

[22] G. A. Victor and A. Dalgarno, Phys. Rev. Lett. **18**, 1105 (1967).

[23] V. L. Jacobs, Phys. Rev. A **4**, 939 (1971).

[24] G. W. F. Drake, G. A. Victor, and A. Dalgarno, Phys. Rev. **180**, 25 (1969).

[25] M. Mizushima, J. Phys. Soc. Jpn. **21**, 2335 (1966).

[26] R. H. Garstang, Astrophys. J. **148**, 579 (1967).

[27] R. H. Garstang, Publ. Astron. Soc. Pac. **81**, 488 (1969).

[28] G. W. F. Drake, Astrophys. J. **158**, 1199 (1969).

[29] G. W. F. Drake, Astrophys. J. **163**, 439 (1971).

[30] V. L. Jacobs, J. Phys. B **5**, 213 (1972).

[31] H. Gould, R. Marrus, and P. J. Mohr, Phys. Rev. Lett. **33**, 676 (1974).

[32] W. R. Johnson and C. D. Lin, Phys. Rev. A **14**, 565 (1976).

[33] W. R. Johnson, C. D. Lin, and A. Dalgarno, J. Phys. B **9**, L303 (1976).

[34] C. D. Lin, W. R. Johnson, and A. Dalgarno, Phys. Rev. A **15**, 154 (1977).

[35] I. S. Bowen (unpublished), see L. D. Huff and W. V. Houston, Phys. Rev. **36**, 842 (1930).

[36] S. Mrozowski, Z. Phys. **108**, 204 (1938).

[37] P. J. Mohr, in *Beam-Foil Spectroscopy*, edited by I. A. Sellin and D. J. Pegg (Plenum, New York, 1976), Vol. 1 p. 97.

[38] P. Indelicato, F. Parente, and R. Marrus, Phys. Rev. A **40**, 3505 (1989).

[39] C. T. Munger (private communication).

[40] R. Pardo, B. E. Clifft, P. Denhartog, D. Kovar, W. Kutschera, and K. E. Rehm, Nucl. Instrum. Methods A **270**, 226 (1988).

[41] J. F. Ziegler, *Handbook of Stopping Cross Sections for Energetic Ions in all Elements* (Pergamon, New York, 1980).

[42] S. Cheng, H. G. Berry, R. W. Dunford, D. S. Gemmell, E. P. Kanter, B. J. Zabransky, A. E. Livingston, L. J. Curtis, J. Bailey, and J. A. Nolen, Jr., Phys. Rev. A **47**, 903 (1993).

[43] L. C. Biedenharn and M. E. Rose, Rev. Mod. Phys. **25**,

729 (1953).

[44] J. F. Williams, M. Kumar, and A. Stelbovics, Phys. Rev. Lett. **70**, 1240 (1993).

[45] C. D. Lin and J. M. Macek, Phys. Rev. A **35**, 5005 (1987).

[46] H. A. Bethe and E. E. Salpeter, *Quantum Mechanics of One- and Two-Electron Atoms* (Springer-Verlag, Berlin, 1957).

[47] E. Storm and H. I. Israel, Nucl. Data Tables A **7**, 565 (1970).

[48] P. Richard, Phys. Lett. **45A**, 13 (1973).

[49] P. Richard, R. C. Kauffmann, F. F. Hopkins, C. W. Woods, and K. A. Jamison, Phys. Rev. Lett. **30**, 888 (1973).

[50] W. J. Braithwaite, D. L. Matthews, and C. F. Moore, Phys. Rev. A **11**, 1267 (1975).

[51] R. W. Hasse, H. D. Betz, and F. Bell, J. Phys. B **12**, L711 (1979).

[52] R. Marrus, P. Charles, P. Indelicato, L. de Billy, C. Tazi, J. Briand, A. Simionovici, D. D. Dietrich, F. Bosch, and D. Liesen, Phys. Rev. A **39**, 3725 (1989).

[53] R. W. Dunford, D. A. Church, C. J. Liu, H. G. Berry, M. L. A. Raphaelian, M. Hass, and L. J. Curtis, Phys. Rev. A **41**, 4109 (1990).

[54] H. G. Berry, R. W. Dunford, and A. E. Livingston, Phys. Rev. A **47**, 698 (1993).

[55] G. W. F. Drake, Can. J. Phys. **66**, 586 (1988).

[56] W. R. Johnson and J. Sapirstein, Phys. Rev. A **46**, 2197 (1992).

[57] M. H. Prior, Phys. Rev. Lett. **29**, 611 (1972).

[58] E. A. Hinds, J. E. Clendenin, and R. Novick, Phys. Rev. A **17**, 670 (1978).

[59] H. Gould and R. Marrus, Phys. Rev. A **28**, 2001 (1983).

[60] C. L. Cocke, B. Curnutte, J. R. MacDonald, J. A. Bednar, and R. Marrus, Phys. Rev. A **9**, 2242 (1974).

[61] R. Marrus and R. W. Schmieder, Phys. Rev. A **5**, 1160 (1972).

[62] G. Feinberg and M. Y. Chen, Phys. Rev. D **10**, 190 (1974).

[63] R. W. Dunford and R. R. Lewis, Phys. Rev. A **23**, 10 (1981).

[64] B. Sakitt and G. Feinberg, Phys. Rev. **151**, 1341 (1966).

[65] R. W. Dunford, H. G. Berry, S. Cheng, E. P. Kanter, C. Kurtz, B. J. Zabransky, A. E. Livingston, and L. J. Curtis, Phys. Rev. A **48**, 1929 (1993).

[66] L. C. Northcliffe and R. F. Schilling, Nucl. Data Tables A

7, 233 (1970).

[67] E. M. Purcell, Astrophys. J. **116**, 457 (1952).

[68] W. M. Goss and G. B. Field, Astrophys. J. **151**, 177 (1968).

[69] I. C. Percival and D. Richards, J. Phys. B **12**, 2051 (1979).

[70] M. J. Seaton, Proc. Phys. Soc. London Sect. A **68**, 457 (1955).

[71] M. J. Seaton, Proc. Phys. **30**, 979 (1958).

[72] L. R. Wilcox and W. E. Lamb, Phys. Rev. **119**, 1915 (1960).

[73] P. Indelicato (private communication). In the notation of R. Marrus, A. Simionovici, P. Indelicato, D. D. Dietrich, P. Charles, J.-P. Briand, K. Finlayson, R. Bosch, D. Liesen, and F. Parente, Phys. Rev. Lett. **63**, 502 (1989), the matrix elements and level widths for ^{61}Ni^{26+} are given by $W_{11} = -0.0109$ eV, $W_{10} = -0.0057$ eV, $\Gamma_0 = 2.640 \times 10^{-7}$ eV, and $\Gamma_1 = 0.0518$ eV.

[74] Our own calculation, based on the formulation of Ref. [37] and the energy-level calculations given in Ref. [55].

[75] H. Krüger and A. Oed, Phys. Lett. **54A**, 251 (1975).

[76] C. A. Kocher, J. E. Clendenin, and R. Novick, Phys. Rev. Lett. **29**, 615 (1972).

[77] A. S. Pearl, Phys. Rev. Lett. **24**, 703 (1970).

[78] R. S. Van Dyck, Jr., C. E. Johnson, and H. A. Shugart, Phys. Rev. A **4**, 1327 (1971).

[79] M. H. Prior and H. A. Shugart, Phys. Rev. Lett. **27**, 902 (1971).

[80] R. Marrus, V. S. Vicente, P. Charles, J. P. Briand, F. Bosch, D. Liesen, and I. Varga, Phys. Rev. Lett. **56**, 1683 (1986).

[81] J. R. Mowat, P. M. Griffin, H. H. Haselton, R. Laubert, D. J. Pegg, R. S. Peterson, I. A. Sellin, and R. S. Thoe, Phys. Rev. A **11**, 2198 (1975).

[82] L. Engström, C. Jupén, B. Denne, S. Huldt, W. T. Meng, P. Kaijser, U. Litzén, and I. Martinson, J. Phys. B **13**, L143 (1980).

[83] B. Denne, S. Huldt, J. Pihl, and R. Hallin, Phys. Scr. **22**, 45 (1980).

[84] A. E. Livingston and S. J. Hinterlong, Nucl. Instrum. Methods **202**, 103 (1982).

[85] C. L. Cocke, B. Curnutte, and R. Randall, Phys. Rev. A **9**, 1823 (1974).

[86] C. L. Cocke, B. Curnutte, J. R. MacDonald, and R. Randall, Phys. Rev. A **9**, 57 (1974).

[87] W. A. Davis and R. Marrus, Phys. Rev. A **15**, 1963 (1977).